

SPECTRAL METHODS FOR TIME-DEPENDENT STUDIES OF ACCRETION FLOWS. III. THREE-DIMENSIONAL, SELF-GRAVITATING, MAGNETOHYDRODYNAMIC DISKS

CHI-KWAN CHAN, DIMITRIOS PSALTIS¹, AND FERYAL ÖZEL
 Physics Departments, University of Arizona, 1118 E. 4th St., Tucson, AZ 85721
Draft version April 15, 2018

ABSTRACT

Accretion disks are three-dimensional, turbulent, often self-gravitating, magnetohydrodynamic flows, which can be modeled in detail with numerical simulations. In this paper, we present a new algorithm that is based on a spectral decomposition method to simulate such flows. Because of the high order of the method, we can solve the induction equation in terms of the magnetic potential and, therefore, ensure trivially that the magnetic fields in the numerical solution are divergence free. The spectral method also suffers minimally from numerical dissipation and allows for an easy implementation of models for sub-grid physics. Both properties make our method ideal for studying MHD turbulent flows such as those found in accretion disks around compact objects. We verify our algorithm with a series of standard tests and use it to show the development of MHD turbulence in a simulation of an accretion disk. Finally, we study the evolution and saturation of the power spectrum of MHD turbulence driven by the magnetorotational instability.

Subject headings: accretion disks — black hole physics — hydrodynamics — magnetohydrodynamics

1. INTRODUCTION

Although the standard accretion disk model was proposed more than thirty years ago (Shakura & Sunyaev 1973), the properties of turbulent angular momentum transport in accretion disks are still not well understood. Shakura & Sunyaev (1973) hypothesized in their original work that magnetic fields may be important in mediating the required angular momentum transport. However, it was not until the last decade that Balbus & Hawley (1991a,b) pointed out that the magnetorotational instability (MRI) generates turbulence and leads to transport of angular momentum in accretion disks.

The non-linear evolution of the MRI and the generation of turbulence was studied numerically by Balbus & Hawley (1991b), following the earlier linear analysis of the instability. Later, local numerical simulations were performed in the shearing box approximation (e.g., Hawley et al. 1995; Brandenburg et al. 1995; Hawley et al. 1996), aimed to study further the local properties of three-dimensional MRI, with and without stratification (Stone et al. 1996). The natural extension of shearing box calculations, namely the cylindrical disks with vanishing vertical gravitational force, were simulated by Hawley (2001); Armitage et al. (2001) to illustrate some important aspects of the turbulent transport, especially in the vicinity of the innermost stable circular orbit around a black hole. Finally, global numerical simulations of MHD disks have also been carried out for a variety of settings and physical conditions.

All of the codes that have been used to study the properties of MRI-driven turbulence have been based on two types of differencing schemes. The first class of studies make use of the very successful scheme developed originally for the ZEUS code (e.g., Stone & Pringle 2001; Armitage et al. 2001; see Stone & Norman 1992a and 1992b for the ZEUS code) or schemes based on it (e.g., Hawley 2000; De Villiers & Hawley 2003; Steinacker & Papaloizou 2002; Igumenschev et al. 2003). The other class of studies have used different conservative schemes (e.g., Koide et al. 1999; Gammie et al. 2003; Machida & Matsumoto 2003). Both types of finite differ-

ence methods allow for a stable and efficient implementation of solvers of the MHD equations. However, they also introduce a considerable amount of numerical dissipation to the problem. This is significant because most calculations have been performed for ideal MHD and, hence, it is this numerical dissipation that allows for the MRI instability to saturate and the resulting turbulence to reach a dynamical steady state (see, however, Flemming, Stone, & Hawley 2000 where the assumption of ideal MHD is relaxed). As a result, the kinetic and magnetic energies of different simulations saturate at different levels depending on the resolution and the scheme (Hawley et al. 1999). The effect of this shortcoming can be reduced, e.g., by increasing the resolution, by increasing the discretization order, or by using numerical schemes that reduce numerical diffusion (see, e.g., Gardiner & Stone 2005, for an unsplit Godunov MHD code).

In this third paper of the series, we address this issue by developing a version of our pseudo-spectral numerical algorithm to simulate three-dimensional MHD disks. Spectral algorithms are high order numerical methods, in which dynamical variables are evolved along orthogonal modes. For smooth functions, they require only $\sim \pi$ grid points to accurately resolve one wavelength, compared to ~ 16 grid points for finite difference schemes to reach the same accuracy. Moreover, the MHD equations can be evolved in time in terms of the vector potential \mathbf{A} , preserving thus trivially the cylindrical character of the magnetic field.

The high order of spectral methods makes them ideal for studying problems of magnetohydrodynamic turbulence, since they do not suffer from serious numerical dissipation. Moreover, spectral methods can easily incorporate models of sub-grid physics, such as the those involved in large-eddy simulation (see, e.g., Blackburn & Schmid 2003). The idea of large-eddy-simulations is to model approximately the small-scale structures, instead of resolving all features of a turbulent flow (see, e.g., Sagaut 2004), with sub-grid models that are based either on experiments or phenomenological descriptions of the small-scale physics. The large-eddy-simulation approach fits naturally to spectral methods because the scale-separation operation is mathematically a fre-

¹ Also Astronomy Department, University of Arizona

quency low-pass filter, which is easily incorporated in a spectral scheme.

In the next section we present the system of equations we solve. In particular, we describe our treatment of the induction equation in terms of the vector potential, in which we introduce an appropriate gauge to avoid the unbounded (linear) growth in the vector potential in a Keplerian flow. In §3 we describe the numerical technique we use. In §4, we present a series of tests to verify the implementation of our algorithm and conclude, in §5, with an application of our method to the study of MHD turbulence in accretion disks driven by the magnetorotational instability.

2. EQUATIONS AND ASSUMPTIONS

Magnetohydrodynamics.—We consider three dimensional viscous, compressible, magnetohydrodynamic flows. The MHD equations contain four equations, namely, the continuity equation

$$\frac{\partial \rho}{\partial t} + \nabla \cdot (\rho \mathbf{v}) = 0, \quad (1)$$

the momentum equation

$$\rho \frac{\partial \mathbf{v}}{\partial t} + \rho (\mathbf{v} \cdot \nabla) \mathbf{v} = -\nabla \left(P + \frac{B^2}{8\pi} \right) + \frac{1}{4\pi} (\mathbf{B} \cdot \nabla) \mathbf{B} + \nabla \tau + \rho \mathbf{g}, \quad (2)$$

the energy equation

$$\frac{\partial E}{\partial t} + \nabla \cdot (E \mathbf{v}) = -P \nabla \cdot \mathbf{v} + \Phi_\nu + \Phi_B - \nabla \cdot \mathbf{q} - \nabla \cdot \mathbf{F}, \quad (3)$$

and the induction equation

$$\frac{\partial \mathbf{A}}{\partial t} = \mathbf{v} \times (\nabla \times \mathbf{A}) + \frac{c^2}{4\pi\sigma} \nabla^2 \mathbf{A} + \nabla \dot{\Lambda}. \quad (4)$$

We denote by ρ the density, by \mathbf{v} the velocity, and by E the thermal energy. In the momentum equation, P is the thermal pressure, τ is the viscosity tensor, and \mathbf{g} is the gravitational acceleration. In the energy equation, there are two dissipative terms, namely, the Ohmic dissipation Φ_η and the viscous dissipation Φ_ν . We use \mathbf{q} to denote the heat flux vector and \mathbf{F} to denote the radiation flux.

We write the induction equation in terms of the vector potential \mathbf{A} , so that the magnetic field is given by $\mathbf{B} = \nabla \times \mathbf{A}$. The symbol σ here represents the electrical conductivity and we define the microscopic resistance by $\eta \equiv c^2/4\pi\sigma$. The last term, $\nabla \dot{\Lambda}$, in the induction equation is a gauge source/sink term, the purpose of which we explain below.

It is straightforward to show that equation (4) leads to the standard induction equation

$$\frac{\partial \mathbf{B}}{\partial t} = \nabla \times (\mathbf{v} \times \mathbf{B}) + (\nabla \cdot \eta \nabla) \mathbf{B}. \quad (5)$$

Because $\nabla \times (\nabla \dot{\Lambda}) \equiv 0$, $\nabla \dot{\Lambda}$ does not affect the magnetic field. However, we retain this gauge term because, by proper choice, it can be used to suspend a non-physical (i.e., numerical) linear growth in \mathbf{A} and hence improve the accuracy of the scheme. To illustrate this, we consider a Keplerian disk with a constant vertical magnetic field so that the vector $\mathbf{v} \times \mathbf{B}$ has a non-zero r -component. By assuming $\eta = 0$, the potential form of the induction equation reduces to

$$\frac{\partial A_r}{\partial t} = B_z \sqrt{\frac{GM}{r}} + \frac{\partial \dot{\Lambda}}{\partial r}, \quad (6)$$

where G and M are the gravitational constant and the mass of the central object, respectively. The first term on the right

hand side leads to a linear growth of A_r in time. This growth will never saturate, because the mean of the product $v_\phi B_z$ is always positive. Although the actual value of the magnetic field will not be affected, this growth will lead to a large round off error in A_r if the MHD equations are integrated for a long time. This difficulty can be overcome by setting

$$\dot{\Lambda} \equiv -B_z \int dr \sqrt{\frac{GM}{r}} = -2B_z \sqrt{GMr}, \quad (7)$$

which suppresses the linear growth of the vector potential. In our algorithm, $\dot{\Lambda}$ is calculated dynamically from the values of $\bar{B}_z(t, r)$ and $\bar{v}_\phi(t, r)$, where the over-bars indicate averages over the azimuthal and vertical directions of the disk, respectively.

The analytical forms of the various physical quantities in equations (1) — (3) were given in Chan et al. (2005). Here, we generalize them to three dimensions. The viscosity tensor (in Cartesian coordinates) is

$$\tau_{ij} = 2(\mu_r + \mu_s) e_{ij} + \left(\mu_r + \mu_b - \frac{2}{3} \mu_s \right) (\nabla \cdot \mathbf{v}) \delta_{ij}, \quad (8)$$

where the strain-rate tensor e_{ij} is

$$e_{ij} = \frac{1}{2} \left(\frac{\partial v_i}{\partial x_j} + \frac{\partial v_j}{\partial x_i} \right). \quad (9)$$

The viscous dissipation rate is, therefore,

$$\Phi_\nu = 2(\mu_r + \mu_s) (e_{ij})^2 + \left(\mu_r + \mu_b - \frac{2}{3} \mu_s \right) (\nabla \cdot \mathbf{v})^2. \quad (10)$$

Finally, the Ohmic dissipation rate, Φ_η , is given by

$$\Phi_\eta = \frac{J^2}{\sigma} = \frac{\eta}{4\pi} |\nabla \times \mathbf{B}|^2. \quad (11)$$

We again assume an ideal gas law so that

$$E = \rho \frac{3k_B T}{2\mu m_H}, \quad (12)$$

$$P = \rho \frac{k_B T}{\mu m_H}. \quad (13)$$

For the induction equation, we typically set the resistance η to zero so that the diffusion term in the induction equation vanishes.

Gravity.—We solve for the gravitational acceleration, \mathbf{g} , in a similar way as in Chan et al. (2006). We first define the gravitational potential Ψ by

$$\mathbf{g} \equiv -\nabla \Psi, \quad (14)$$

which is given by the volume integral

$$\Psi(t, \mathbf{x}) = -G \int \frac{\rho(t, \mathbf{x}')}{|\mathbf{x} - \mathbf{x}'|} d^3 x' \quad (15)$$

over all space. Rewriting equation (15) in differential form, we obtain Poisson's equation

$$\nabla^2 \Psi = 4\pi G \rho, \quad (16)$$

with Ψ satisfying the boundary condition $\Psi(t, \infty) = 0$ at all times. When simulating accretion flows, the computational domain $\mathcal{D}^{(3)}$ is usually finite. Based on its linearity, we can decompose Poisson's equation into two parts, i.e.,

$$\nabla^2 \Psi_{\text{int}} = 4\pi G \rho_{\text{int}}, \quad (17)$$

and

$$\nabla^2 \Psi_{\text{ext}} = 4\pi G \rho_{\text{ext}}, \quad (18)$$

where ρ_{int} denotes the mass density within the computational domain, which in our case is the disk density, and ρ_{ext} refers to external sources such as the central object and/or a companion star. The gravitational field is then given by

$$\mathbf{g} = \mathbf{g}_{\text{int}} + \mathbf{g}_{\text{ext}} = -\nabla(\Psi_{\text{int}} + \Psi_{\text{ext}}). \quad (19)$$

For the gravitational field of the central object, we use the pseudo-Newtonian approximation of Mukhopadhyay (2002) for \mathbf{g}_{ext} , which takes the form

$$\mathbf{g}_{\text{ext}} = -\frac{c^2}{r^3} \left(\frac{GM}{c^2} \right)^2 \left[\frac{r^2 - 2(a/c) \sqrt{GMr/c^2} + (a/c)^2}{\sqrt{GMr/c^2}(r-r_S) + a/c} \right]^2 \hat{\mathbf{r}}. \quad (20)$$

Here, $r_S \equiv 2GM/c^2$ is the Schwarzschild radius and a is a parameter related to the spin of the central object.

In order to solve for self-gravity using equation (17) within $\mathcal{D}^{(3)}$, we compute the integral

$$\Psi_{\text{int}}(t, \mathbf{x}) = -G \int_{\mathcal{D}^{(3)}} \frac{\rho_{\text{int}}(t, \mathbf{x}')}{|\mathbf{x} - \mathbf{x}'|} d^3 x', \quad (21)$$

as in Chan et al. (2006). We then use equation (19) to obtain the total gravitational field and use it in the momentum equation.

Subgrid Physics.—For homogeneous and isotropic turbulence, the ratio between the most energetic scale to the viscous length scale is proportional to $\mathcal{O}(Re^{3/4})$, where Re is the Reynolds number. This scaling law suggests that the computational cost is proportional to $\mathcal{O}(Re^3)$ for three-dimensional, time-dependent simulations. Although spectral methods offer efficient ways to capture small scale features, they are still unable to resolve, even in the shearing box approximation, the expected dynamical range in accretion disks down to the molecular viscous length scale.

In order to reduce the computational cost, we need to introduce an artificial cut-off to the problem. Following the Large Eddy Simulation approach (LES, see Sagaut 2004, for a very detailed introduction), we will use our numerical algorithm to solve the MHD equations for scales larger than this cut-off scale and introduce an approximate model for the smaller scales. Introducing such a model is required by the non-linear character of the MHD equations, which allow for coupling between the simulated large scales and the unresolved small scales.

For any physical quantity f , we denote by \bar{f} the filtered (i.e., resolved) function and define the sub-grid fluctuation by

$$f' \equiv f - \bar{f}. \quad (22)$$

We can then formally decompose any non-linear product of two physical quantities fg in physical space as

$$\begin{aligned} \bar{f}\bar{g} &= \overline{(\bar{f} + f')(\bar{g} + g')} \\ &= \bar{f}\bar{g} + L_{ij} + C_{ij} + R_{ij}, \end{aligned} \quad (23)$$

where

$$\begin{aligned} L_{ij} &= \bar{\bar{f}}\bar{g} - \bar{f}\bar{g}, \\ C_{ij} &= \bar{f}\bar{g}' + \bar{f}'\bar{g}, \\ R_{ij} &= \bar{f}'\bar{g}'. \end{aligned} \quad (24)$$

If the quantities f and g are different components of the velocity, these higher order correlations are the Leonard tensor, the

cross-stress tensor, and the Reynolds sub-grid tensor, respectively (Sagaut 2004). Note that the Reynolds sub-grid tensor is different from the (physical) Reynolds stress tensor. It appears because of the presence of the artificial cut-off and is independent of the molecular viscosity.

The basic idea of Large Eddy Simulations is to devise a model for the three tensors (24) that captures the physics of sub-grid turbulence. This is beyond the scope of the current paper. Here, we will approximate the sum $L_{ij} + C_{ij} + R_{ij}$ in spectral space by the the spectral filter (Chan et al. 2005)

$$\sigma_{\beta} \left(\frac{n}{N} \right) = \exp \left(-|\ln \epsilon| \left| \frac{n}{N} \right|^{\beta} \right), \quad (25)$$

where β is the order of the filter; ϵ is the machine accuracy, which is of order 10^{-15} for double precision floating point numbers; and n and N are the point index and number of points in spectral space, respectively. Applying this filter once after every timestep is equivalent to adding a high-order (super) diffusion term in the dynamic equations. Although this approach is not based on any physical model, it has been known to reproduce the large-scale properties of turbulent flows (e.g., Karamanos & Karniadakis 2000; Pasquetti 2005).

3. IMPLEMENTATION OF THE PSEUDO-SPECTRAL METHODS

In our current implementation of the pseudo-spectral method in three-dimensions we use cylindrical coordinates because we are interested in the study of geometrically thin accretion disks. It is trivial, however, to alter the geometry of the domain of solution, when necessary, and use spherical-polar coordinates.

Along the radial direction, we use a Chebyshev collocation method, whereas, for the azimuthal and vertical directions, we choose the Fourier basis. This implies periodic boundary conditions for both the azimuthal direction (which is natural) and the vertical direction (which needs to be justified for each specific application). The computational domain is $\mathcal{D}^{(3)} = [r_{\min}, r_{\max}] \times [-\pi, \pi] \times [-Z, Z]$ and we require $r_{\min} > 0$ to avoid the coordinate singularity at the origin.

Formally, we expand any physical quantity $f(t, r, \phi, z)$ as

$$f(t, r, \phi, z) = \sum_{n,m,l} \check{f}_{nml}(t) T_n(\bar{r}) e^{im\phi} e^{i\pi lz/Z}. \quad (26)$$

Here T_n is the n -th order Chebyshev polynomial and $\bar{r} \in [-1, 1]$ is the standardized coordinate in the radial direction (Chan et al. 2005). Note that the frequently used Chebyshev-Gauss-Lobatto grid

$$\bar{r}_k \equiv \cos \left(\frac{\pi k}{N} \right), \text{ for } 0 \leq k \leq N \quad (27)$$

has the property that

$$\bar{r}_0 - \bar{r}_1 = \bar{r}_{N-1} - \bar{r}_N \propto N^{-2}. \quad (28)$$

This gives the time-stepping constrain $\Delta t \propto N^{-2}$ for hyperbolic (wave-like) equations and $\Delta t \propto N^{-4}$ for parabolic (diffusion-like) equations. To overcome this restriction, we use instead the Kosloff-Tal-Ezer mapping (Kosloff & Tal-Ezer 1993)

$$r = \frac{r_{\max}}{2} \left[\frac{\arcsin(\alpha \bar{r})}{\arcsin(\alpha)} + 1 \right] - \frac{r_{\min}}{2} \left[\frac{\arcsin(\alpha \bar{r})}{\arcsin(\alpha)} - 1 \right]. \quad (29)$$

We choose the parameter α , which controls the regularity of the grid spacing, to be $\text{sech}(|\ln \epsilon|/N)$, where ϵ is the machine accuracy, to optimize the accuracy of the spatial derivatives (Don & Solomonoff 1997).

We compute the numerical derivatives along the r - and ϕ -directions as in Chan et al. (2005, 2006). Hence, the radial derivative is given by the chain rule

$$\frac{\partial f}{\partial r} = \frac{1}{dr/d\bar{r}} \frac{\partial f}{\partial \bar{r}}, \quad (30)$$

where the derivative in the standardized coordinate is

$$\frac{\partial f}{\partial \bar{r}} = \sum_{n,m,l} \check{f}_{nml}^{(1)}(t) T_n(\bar{r}) e^{im\phi} e^{i\pi lz/Z}. \quad (31)$$

We precompute analytically the derivative of the mapping, $dr/d\bar{r}$. Here, we use $\check{f}^{(1)}$ to denote the Chebyshev coefficient of the radial derivative and compute it using the following three-term recursive relation

$$\check{f}_{N,m,l}^{(1)} = 0, \quad (32)$$

$$\check{f}_{N-1,m,l}^{(1)} = 2N \check{f}_{N,m,l}, \quad (33)$$

$$c_n \check{f}_{n,m,l}^{(1)} = \check{f}_{n+2,m,l}^{(1)} + 2(n+1) \check{f}_{n+1,m,l}, \quad (34)$$

where $c_0 = 2$ and $c_n = 1$ for $n = 1, 2, \dots, N$. The azimuthal derivative is given by

$$\frac{\partial f}{\partial \phi} = \sum_{n,m,l} im \check{f}_{nml}(t) T_n(\bar{r}) e^{im\phi} e^{i\pi lz/Z}. \quad (35)$$

Finally, the derivative along the z -direction is similar to the azimuthal derivative except for the extra normalization π/Z , i.e.,

$$\frac{\partial f}{\partial z} = \sum_{n,m,l} \frac{i\pi l}{Z} \check{f}_{nml}(t) T_n(\bar{r}) e^{im\phi} e^{i\pi lz/Z}. \quad (36)$$

4. CODE VERIFICATION

We have verified our numerical algorithm using a suit of test problems, some of which we present in this section. For a test particular to the three-dimensional hydrodynamics, we adopt the free-falling dust ring test from Chan et al. (2005); for MHD, we study the magnetic braking of a rotating slab, following Stone et al. (1992).

4.1. An Advection Test: Free Fall of a Dust Ring

Following Chan et al. (2005), we use a free falling dust ring as an advection test of our three-dimensional algorithm. The computational domain is $[0.2, 1.8] \times [-\pi, \pi] \times [-1, 1]$ with $65 \times 32 \times 65$ collocation points. The initial density is the Gaussian

$$\rho_0 = \exp[-20(r-1)^2 - 20z^2]. \quad (37)$$

In order to also test the advection along the z -direction, we set the initial velocity to $\mathbf{v} = (0, 0, 1)$, which is equivalent with performing this test on a non-stationary Galilean frame. We assume that the gravitational acceleration is Newtonian and that of a central external object, i.e., that $\mathbf{g} = (-1/r^2, 0, 0)$. (Note that, for a cylindrically symmetric central object, the gravitational field should have been proportional to $1/r$.) We also neglect pressure and magnetic fields in this test.

The analytical solution of this test is found in the same way as is Chan et al. (2005). Because the initial vertical velocity is non-zero, we have to replace z by $z - v_z t$ in order to capture the vertical motion. The analytical solution, therefore, reads

$$\Sigma(t, r, \phi, z) = \Sigma_0(r_0, z - v_z t) \frac{r_0^2}{r} \left[\frac{3t}{2} \sqrt{\left(\frac{2}{r_0} \right) \left(\frac{r_0}{r} - 1 \right) + r} \right]^{-1} \quad (38)$$

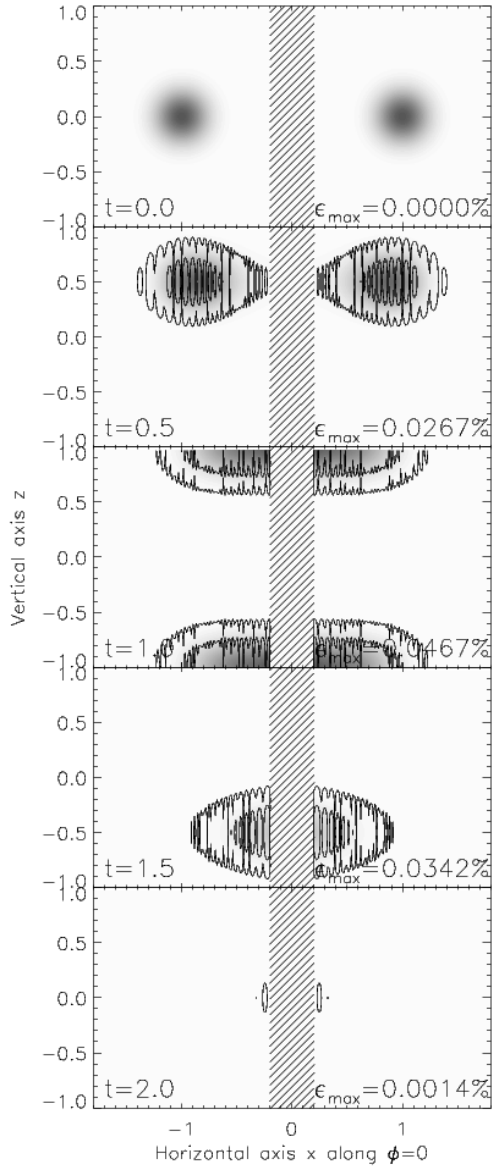


FIG. 1.— A comparison of the numerical to the analytical solution for the free-falling dust ring test problem discussed in the text. The gray-scale image depicts the density profile at different times in the simulation. The contour lines show the positions in the solution domain where the fractional error between the numerical and analytical solutions are 0.01% and 0.001%. In all plots, we also show the maximum error ϵ_{\max} for reference.

where r_0 is found by solving implicitly the equation

$$\frac{\sqrt{2}}{r_0^{3/2}} t = \frac{1}{2} \sin \left(2 \arccos \sqrt{\frac{r}{r_0}} \right) + \arccos \sqrt{\frac{r}{r_0}}. \quad (39)$$

In Figure 1, we plot the numerical density as gray-scale contours at $\phi = 0$ and for different times. The error between the numerical solution and the analytical solution is overplotted as a set of contour lines. The maximum error throughout the simulation is of order 10^{-4} . Note that our implementation of the free-streaming inner boundary condition does not introduce any significant errors caused by the artificial excitation or reflection of waves.

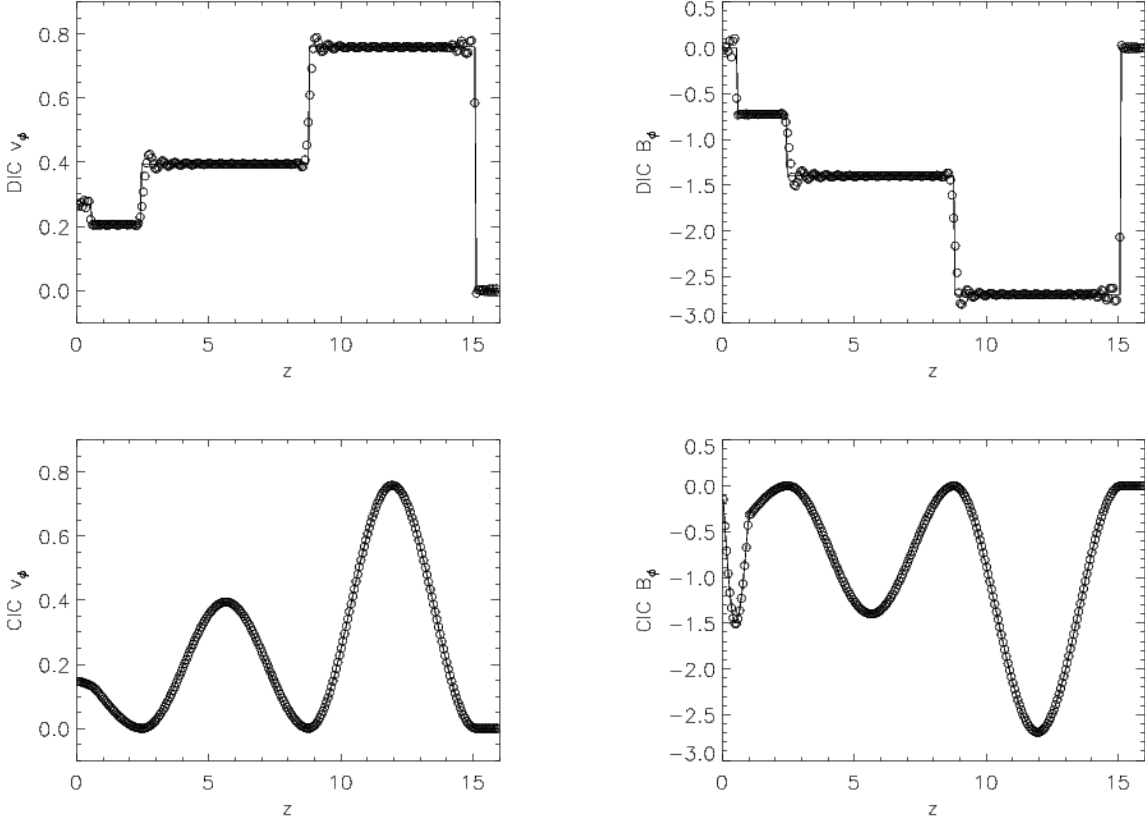


FIG. 2.— A comparison of the numerical (circles) to the analytical (lines) solutions for the magnetic breaking test problem. The panels show a snapshot of the azimuthal velocity and magnetic field at time $t = 50$, for the discontinuous (DIC; upper panels) and the continuous (CIC; lower panel) initial conditions discussed in the text. For the discontinuous case, the numerical solution captures correctly the shock properties despite the Gibbs oscillations; for the continuous case, the numerical and analytical solutions are indistinguishable.

4.2. A Test of Alfvén Wave Propagation: Magnetic Braking of an Aligned Rotator

The problem of magnetic breaking of an aligned rotator via the emission of nonlinear, incompressible Alfvén waves was solved analytically by Mouschovias & Paleologou (1980). It was then used by Stone et al. (1992) to verify the ability of MHD algorithms to propagate transverse Alfvén waves. In this test, we use the same initial conditions as those described by Stone et al. (1992), namely, the discontinuous initial condition (DIC) and the continuous initial condition (CIC). Because our algorithm is designed for compressible MHD flows, we discard the radial and vertical components of the momentum equation and set $\partial P / \partial \phi = 0$ in the azimuthal component.

We use the computational domain $[0.2, 1.8] \times [-\pi, \pi] \times [-16, 16]$ with $33 \times 32 \times 512$ collocation points. We set the initial density to

$$\rho_0 = \begin{cases} 1 & , |z| > 1 \\ 10 & , \text{otherwise} \end{cases} \quad (40)$$

the initial magnetic field to $\mathbf{B} = (0, 0, 1)$, and the initial velocity to $\mathbf{v} = (0, r\Omega_0, 0)$ where Ω_0 is the initial angular velocity. For the discontinuous case (DIC), we set the angular velocity to

$$\Omega_0 = \begin{cases} 0 & , |z| > 1 \\ 1 & , \text{otherwise}, \end{cases} \quad (41)$$

whereas for the continuous case (CIC) we set it to

$$\Omega_0 = \begin{cases} 0 & , |z| > 1 \\ \frac{1}{2}(1 + \cos \pi z) & , \text{otherwise}. \end{cases} \quad (42)$$

The analytic solutions are given in Mouschovias & Paleologou (1980).

In Figure 2, we compare the numerical to the analytical solutions for the two initial conditions at $t = 50$, right before the wave front passes $z = 16$. The numerical solution for the discontinuous problem shows oscillations around the discontinuity (the Gibbs phenomenon), which are inherent to all spectral methods. However, the properties of the shock as well as those of the fluid around it are captured correctly in our numerical solutions. For the continuous problem, the numerical and analytical solutions are indistinguishable.

5. TURBULENT MHD DISKS DRIVEN BY THE MAGNETO-ROTATIONAL INSTABILITY

One of the advantages of spectral methods is the fact that they allow for an accurate control of numerical dissipation and hence they can be used to track accurately the stability of a flow. In Chan et al. (2005) we used our two-dimensional, hydrodynamic spectral algorithm to successfully reproduce the Rayleigh stability criterion in a couette flow, even near the separatrix. In Chan et al. (2006) we applied our spectral algorithm to self-gravitating disks and studied Toomre's criterion. In this section, we use our MHD spectral algorithm to study the properties of accretion disks driven by the magnetorotational instability (MRI) (Balbus & Hawley 1991a).

Any ionized and magnetized accretion disk is unstable to the MRI as long as the angular velocity of the flow is a decreasing function of radius. If a cylindrical disk is threaded by a mean vertical magnetic field B_z , all the waves along the

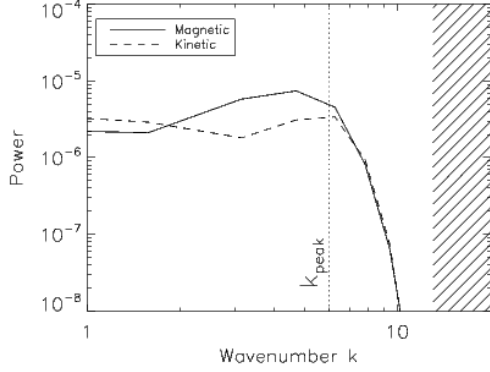


FIG. 3.— The power spectrum along the vertical direction of the magnetic and kinetic turbulent energies in a Keplerian disk at $r = 20$, during the exponential growth of the MRI (at $t = 200$), for the simulation discussed in the text. The hash-filled area represents the limit of the numerical resolution. The vertical dotted line corresponds to the wavenumber of the most unstable mode as predicted by the analysis of the linear MRI.

vertical direction with wavenumbers less than

$$k_{\text{MRI}} = \sqrt{2q} \frac{\Omega}{v_A}, \quad (43)$$

are unstable. Here, Ω is the angular frequency,

$$q \equiv -\frac{d \ln \Omega}{d \ln r} \quad (44)$$

is a measure of the shear, and $v_A = B_z / \sqrt{4\pi\rho}$ is the Alfvén velocity for the background field. The growth rate of the instability depends strongly on the wavenumber and is given by (Balbus & Hawley 1991a)

$$\gamma = \left[-(2-q) - k^2 + \sqrt{(2-q)^2 + 4k^2} \right]^{1/2} \Omega. \quad (45)$$

The fastest growing mode has a wavenumber given by

$$k_{\text{peak}} = \frac{q}{2} \left(\frac{4}{q} - 1 \right)^{1/2} \frac{\Omega}{v_A}. \quad (46)$$

We use our numerical algorithm to simulate the evolution of a Keplerian disk in a pseudo-Newtonian potential around a non-rotating object of mass M . For this calculation, we set $G = c = 1$ and all the distances and times in gravitational units. We solve the MHD equations in the computational domain $[3, 43] \times [-\pi, \pi] \times [-2, 2]$ using $257 \times 64 \times 32$ grid points. In order to justify the periodic boundary conditions along the vertical direction and avoid numerical problems around the innermost stable circular orbit, we set the sound speed to $c_s^2 \approx 0.2$. We set the initial density to unity everywhere in the disk and thread the flow with a vertical magnetic field with a corresponding Alfvén velocity equal to 2×10^{-3} . In our dimensionless units, it takes a time of $t \approx 60$ and $t \approx 500$, respectively, for the fluid elements to complete one orbit at $r = 6$ and $r = 20$.

The initial exponential growth of the MRI offers another possibility to test the ability of our numerical method to capture the properties of an MHD instability. For this reason, we discuss first the initial stages of the simulation and then the properties of the final state of saturated MHD turbulence.

In Figure 3, we show the power spectrum of the magnetic and kinetic energies in the simulation, at a radius $r = 20$, during the initial linear regime of the instability. The similarity of the peak of the numerical power spectrum to the wavenumber

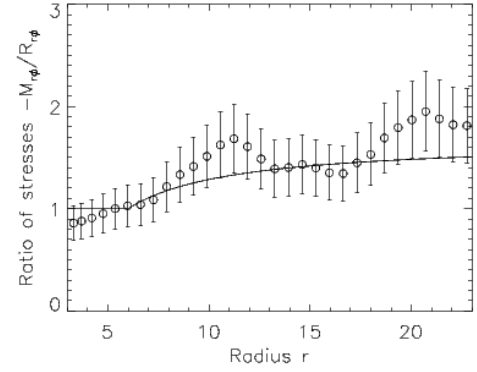


FIG. 4.— The ratio of the $r\phi$ components of the Maxwell, and Reynolds stresses, as a function of radius in the accretion flow at time $t = 2000$. The error bars indicate the $\approx 20\%$ uncertainty in the value of each stress. The solid line shows the result of the analytic calculation for the stress ratio (Pessah et al. 2006).

of the most unstable mode of the linear MRI demonstrates that our numerical algorithm can reproduce, with an uncertainty comparable to the resolution, the wavenumber of the mode that shows the fastest growth rate (eq. [46]).

The Maxwell and Reynolds stresses are amplified exponentially during the initial growth of the instability, with their ratios determined only by the value of local shear (Pessah et al. 2006). In Figure 4, we plot the ratio of the Maxwell to Reynolds stresses as a function of radius in the accretion disk at time $t = 200$ and compare it to the analytical solution of Pessah et al. (2006). The numerical and analytical ratios agree well, within the uncertainties of estimating appropriate averages.

After a few orbital periods, turbulence is generated and the solution of the system of MHD equations becomes highly non-linear. Figure 5 shows the evolution of the density and magnetic energy in the accretion flow from the initial laminar state (first panel), through the time of the exponential growth of the MRI (second panel), to the final saturated state of MHD turbulence (last two panels). As also found in previous simulations of MRI-driven turbulent accretion disks, the solution is highly variable, with large fluctuations in the various physical quantities. Moreover, the magnetic and material stresses are not consistent with the prediction of the alpha model and are non-vanishing inside the innermost stable circular orbit. In this paper, we are particularly interested in the evolution and properties of the power spectrum of turbulence, which is a statistic that spectral methods are primarily suited to calculate.

Figure 6 shows the evolution of the power spectrum along the vertical direction of the magnetic energy at cylindrical radius $r = 20$. At early times, the magnetic energy increases exponentially because of the growth of the MRI, generating a spectrum of fluctuations that peaks around the wavenumber of maximum growth. At later times, interactions between different modes lead to spreading of turbulent energy to nearby modes, generating a power-law spectrum of fluctuations. The index of the power spectrum of magnetic energy fluctuations is comparable to that of a Kolmogorov spectrum, even though the MHD turbulence is highly anisotropic.

The power-law spectrum of magnetic energy fluctuations extends from the largest vertical scale of the simulation (which is the vertical extent of the domain of solution) to the smallest vertical scale (which is equal to the numerical

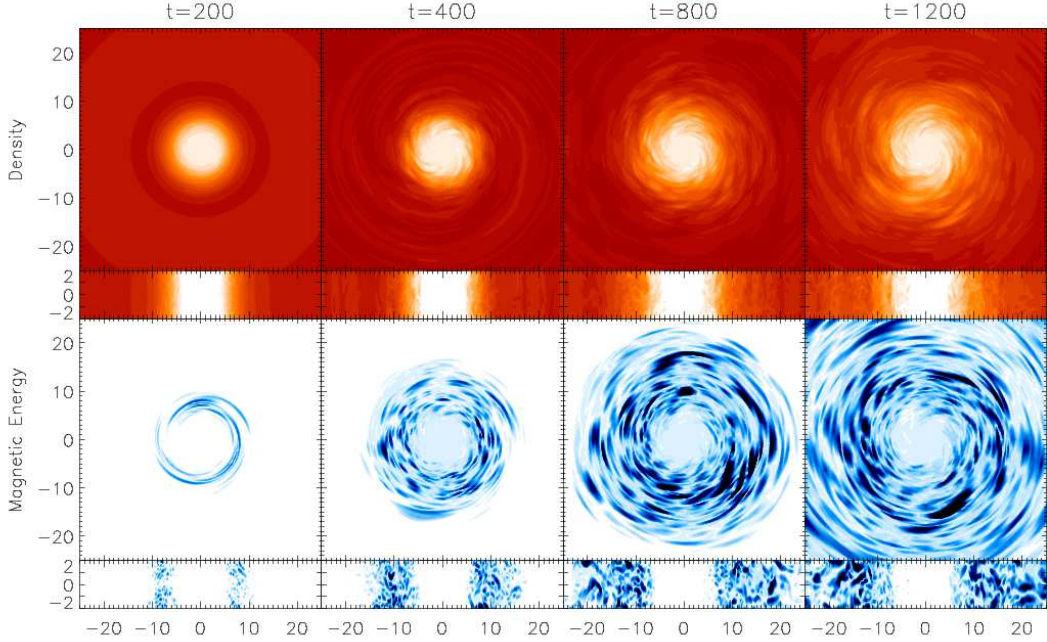


FIG. 5.— Four density (upper rows) and magnetic energy (lower rows) snapshots of the evolution of the MHD turbulence in an accretion disk driven by the magnetorotational instability. The face-on views show the two physical quantities at the midplane of the domain of solution, whereas the edge-on views are for an azimuth of $\phi = 0$. In each row, the first panel corresponds to a state very close to the initial laminar flow; the second panel shows the density during the exponential growth of the MRI; the last two panels show two different instants during the saturated state of the turbulence.

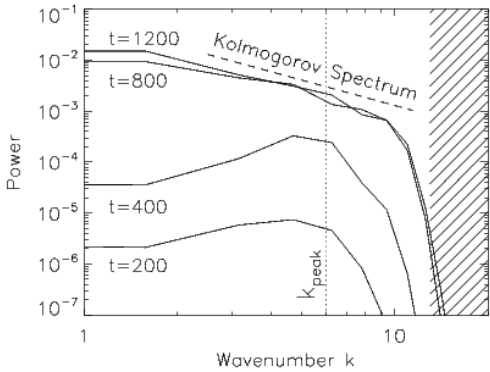


FIG. 6.— The evolution of the power spectrum along the vertical direction of the magnetic energy at cylindrical radius $r = 20$, for the accretion disk simulation shown in Figure 5. The hash-filled area starts at the cut-off wavenumber of the spectral filter and represents the numerical resolution. The vertical dotted line corresponds to the wavenumber of the most unstable mode as predicted by the analysis of the linear MRI.

resolution). Moreover, the integral of the power spectrum, which is equal to the total variance, depends on both scales. This is consistent with the fact that the saturation predictor found in numerical simulations of shearing boxes depends on both the vertical size of the box and the numerical resolution (Hawley et al. 1995, 1996; Pessah et al. 2006b). It is, however, a result of two simplifying assumptions in our simulation. The power spectrum extends to the largest vertical scale because we have neglected the vertical component of gravity and, therefore, the disk is not stratified. At the same time, the power spectrum extends to the smallest resolved scale because we have neglected Ohmic dissipation. Obtaining a realistic saturation predictor of MRI-driven turbulence in accretion disks will require numerical simulations of stratified flows with the largest possible dynamical range and an accurate model of sub-grid physics.

C.-K. C. and D. P. acknowledge support from the NASA ATP grant NAG-513374.

APPENDIX

A. ADVECTIVE-CONSERVATIVE MIXED FORMALISM FOR MHD

As in Chan et al. (2005), we use the non-linear terms $(\mathbf{v} \cdot \nabla) \mathbf{v}$ in their advective forms, whereas we use the terms that involve the density, ρ , and the energy, E , in conservative form. For the vector potential, we use an advective form in order to increase stability. In detail:

$$\partial_t \rho = -\frac{\partial_r(r\rho v_r)}{r} - \frac{\partial_\phi(\rho v_\phi)}{r} - \partial_z(\rho v_z), \quad (A1)$$

$$\begin{aligned} \partial_t v_r = & -v_r \partial_r v_r - \frac{v_\phi}{r} (\partial_\phi v_r - v_\phi) - v_z \partial_z v_r + \frac{\partial_r(r\tau_{rr} - rP - rB^2/8\pi)}{r\rho} + \frac{\partial_\phi \tau_{\phi r}}{r\rho} + \frac{\partial_z \tau_{zr}}{\rho} + \frac{P + B^2/8\pi - \tau_{\phi\phi}}{r\rho} \\ & + \frac{B_r \partial_r B_r}{4\pi\rho} + \frac{B_\phi (\partial_\phi B_r - B_\phi)}{4\pi r\rho} + \frac{B_z \partial_z B_r}{4\pi\rho} + g_r \end{aligned} \quad (A2)$$

$$\begin{aligned} \partial_t v_\phi = & -v_r \partial_r v_\phi - \frac{v_\phi}{r} (\partial_\phi v_\phi + v_r) - v_z \partial_z v_\phi + \frac{\partial_r (r \tau_{r\phi})}{r \rho} + \frac{\partial_\phi (\tau_{\phi\phi} - P - B^2/8\pi)}{r \rho} + \frac{\partial_z \tau_{z\phi}}{\rho} + \frac{\tau_{r\phi}}{r \rho} \\ & + \frac{B_r \partial_r B_\phi}{4\pi \rho} + \frac{B_\phi (\partial_\phi B_\phi + B_r)}{4\pi r \rho} + \frac{B_z \partial_z B_\phi}{4\pi \rho} + g_\phi, \end{aligned} \quad (\text{A3})$$

$$\begin{aligned} \partial_t v_z = & -v_r \partial_r v_z - \frac{v_\phi}{r} \partial_\phi v_z - v_z \partial_z v_z + \frac{\partial_r (r \tau_{rz})}{r \rho} + \frac{\partial_\phi \tau_{\phi z}}{r \rho} + \frac{\partial_z (\tau_{zz} - P - B^2/8\pi)}{r \rho} \\ & + \frac{B_r \partial_r B_z}{4\pi \rho} + \frac{B_\phi \partial_\phi B_z}{4\pi r \rho} + \frac{B_z \partial_z B_z}{4\pi \rho} + g_z, \end{aligned} \quad (\text{A4})$$

$$\partial_t E = -\frac{\partial_r (r E v_r + r q_r + r F_r)}{r} - \frac{\partial_\phi (E v_\phi + q_\phi + F_\phi)}{r} - \partial_z (E v_z + q_z + F_z) - P \left(\partial_r v_r + \frac{\partial_\phi v_\phi + v_r}{r} + \partial_z v_z \right) + \Phi_\nu + \Phi_\eta, \quad (\text{A5})$$

$$\partial_t A_r = v_\phi B_z - v_z B_\phi + \eta \left[\frac{1}{r} \partial_r (r \partial_r A_r) + \frac{1}{r^2} \partial_\phi^2 A_r + \partial_z^2 A_r - \frac{A_r}{r^2} \right] - \partial_r \dot{\Lambda} \quad (\text{A6})$$

$$\partial_t A_\phi = v_z B_r - v_r B_z + \eta \left[\partial_z^2 A_\phi - \frac{A_\phi}{r^2} + \frac{1}{r} \partial_r (r \partial_r A_\phi) + \frac{1}{r^2} \partial_\phi^2 A_\phi \right] - \frac{1}{r} \partial_\phi \dot{\Lambda} \quad (\text{A7})$$

$$\partial_t A_z = v_r B_\phi - v_\phi B_r + \eta \left[\frac{1}{r} \partial_r (r \partial_r A_z) + \frac{1}{r^2} \partial_\phi^2 A_z + \partial_z^2 A_z \right] - \partial_z \dot{\Lambda} \quad (\text{A8})$$

The notation ∂_t denotes partial derivatives with respect to time. We integrate this equations forward in time using a low storage, third-order Runge-Kutta scheme (see Chan et al. 2005, 2006, for detail).

We compute the magnetic field from the vector potential as

$$B_r = \frac{\partial_\phi A_z}{r} - \partial_z A_\phi \quad (\text{A9})$$

$$B_\phi = \partial_z A_r - \partial_r A_z \quad (\text{A10})$$

$$B_z = \frac{\partial_r (r A_\phi)}{r} - \frac{\partial_\phi A_r}{r} \quad (\text{A11})$$

The only non-trivial term here is $\partial_r (r A_\phi)$, which is in conservative form.

The viscosity tensor τ_{ij} in the above equation has the following general form

$$\tau_{ij} = 2(\mu_r + \mu_s) e_{ij} + \left(\mu_r + \mu_b - \frac{2}{3} \mu_s \right) (\nabla \cdot \mathbf{v}) \delta_{ij}. \quad (\text{A12})$$

As we describe before, μ_r , μ_b , and μ_s are the coefficients of radiative, bulk, and shearing viscosity. The strain rate tensor e_{ij} written in cylindrical coordinate becomes

$$e_{rr} = \partial_r v_r \quad (\text{A13})$$

$$e_{\phi\phi} = \frac{\partial_\phi v_\phi}{r} + \frac{v_r}{r} \quad (\text{A14})$$

$$e_{zz} = \partial_z v_z \quad (\text{A15})$$

$$e_{r\phi} = e_{\phi r} = \frac{1}{2} \left(\partial_r v_\phi - \frac{v_\phi}{r} + \frac{1}{r} \partial_\phi v_r \right) \quad (\text{A16})$$

$$e_{\phi z} = e_{z\phi} = \frac{1}{2} \left(\frac{\partial_\phi v_z}{r} + \partial_z v_\phi \right) \quad (\text{A17})$$

$$e_{zr} = e_{rz} = \frac{1}{2} (\partial_z v_r + \partial_r v_z). \quad (\text{A18})$$

The viscous dissipation is

$$\Phi_\nu = 2(\mu_r + \mu_s) (e_{ij})^2 + \left(\mu_r + \mu_b - \frac{2}{3} \mu_s \right) (\nabla \cdot \mathbf{v})^2, \quad (\text{A19})$$

and the Ohmic dissipation rate Φ_η is given by

$$\Phi_\eta = \frac{\eta}{4\pi} \left[\left(\frac{\partial_\phi B_z}{r} - \partial_z B_\phi \right)^2 + (\partial_z B_r - \partial_r B_z)^2 + \left(\frac{\partial_\phi (r B_\phi)}{r} - \frac{\partial_\phi B_r}{r} \right)^2 \right]. \quad (\text{A20})$$

B. CODE PARALLELIZATION

If the magnetohydrodynamic equations were linear, the parallelization of the spectral algorithm would be trivial, because the coefficient of each of the basis polynomials would evolve independently from the others. However, the non-linear terms in the

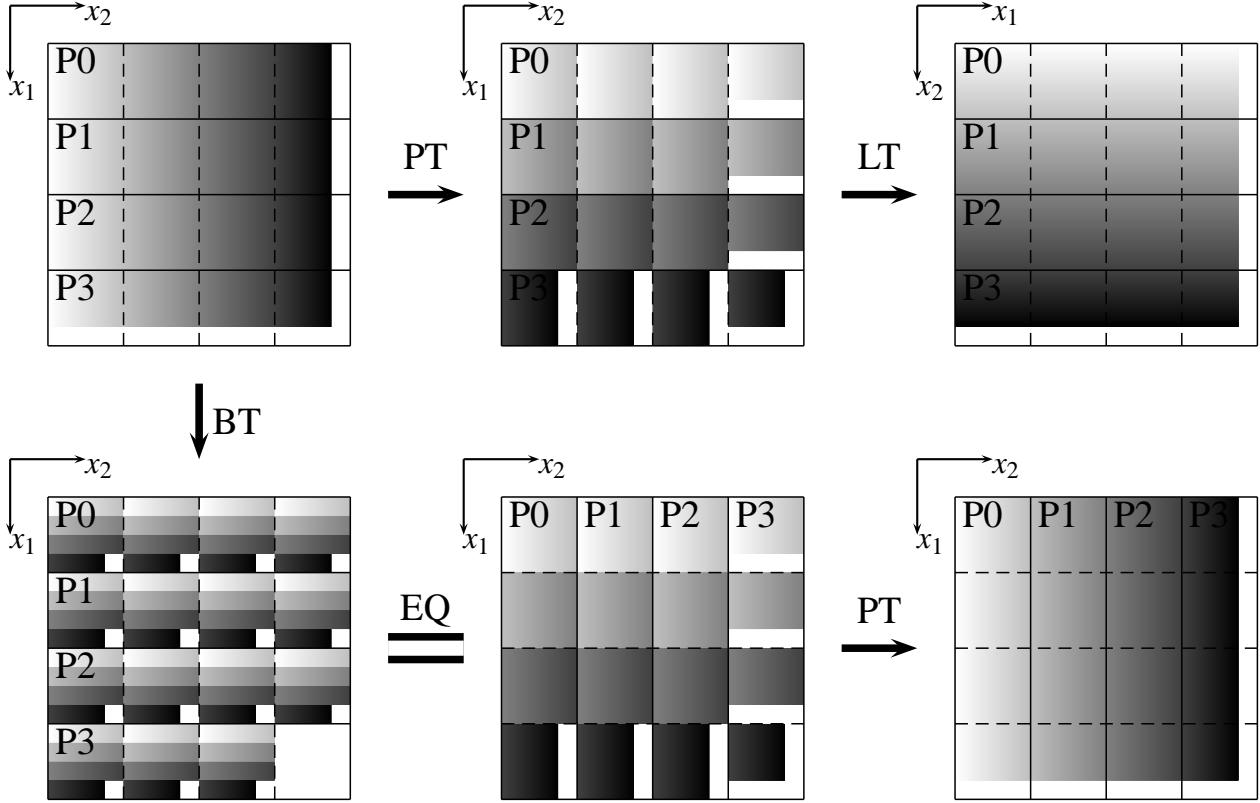


FIG. A1.— Schematic representation of the standard parallel FFT procedure in two dimensions (upper panel) and the alternate flip-flop procedure we have implemented in our algorithm (bottom panel).

equations necessitate cross-processor communication. As discussed in Chan et al. (2005), we incorporate the non-linear terms in the time-stepping by transforming the relevant physical quantities to coordinate space and evaluating the non-linear terms there, before transforming them back to spectral space. The efficient parallelization of our algorithm, therefore, relies on efficiently implementing a parallel version of the Fast Fourier Transform (FFT) algorithm for a multi-dimensional set of grid points. We use the Message Passing Interface (MPI) standard to parallelize our algorithm (see Gropp et al. 1999a,b).

In Figure A1 we present schematically an example of our implementation of the FFT algorithm for transforming the values of a physical quantity on a two-dimensional grid along the x_1 and x_2 directions. The standard algorithm for parallel Fast Fourier Transform starts with an one-dimensional (“slab”) decomposition to distribute the data across different processors. We use solid lines in the figure to denote the distribution of grid points on different processors, which we label by P0, P1, P2, etc. It is clear from the upper-left panel of the figure that applying spectral methods along the x_2 direction is straight forward. We can simply use the ordinary FFT for each row locally. However, for performing an FFT along the x_1 direction, communication between the various processors is necessary. The standard method requires taking first a parallel transpose (PT), exchanging data between processors, and then a local transpose (LT), per processor, as illustrated in the upper panels of Figure A1. These two processes exchange the directions of x_1 and x_2 and FFTs are then applied on each row separately.

We developed an alternate (“flip-flop”) procedure to increase the performance of parallel FFTs in multi-dimensions, by avoiding the time consuming step of obtaining the local transpose on each processor. The lower row of Figure A1 illustrates the flipping procedure, which involves a block transpose (BT) and a parallel transpose (PT) operation. The flopping procedure follows the opposite routine. In these operations we can take advantage of the resulting memory layout and use the cache more efficiently. Because the order of the indices is preserved, the algorithm is easier to implement. More importantly, depending on the domain size and the number of processors we use, this approach can speed up the parallel FFT by $\sim 20\%$ in our 32-processor Beowulf cluster.

REFERENCES

Armitage, P. J., Reynolds, C. S., & Chiang, J. 2001, *ApJ*, 548, 868
 Balbus, S.A. & Hawley, J.F. 1991, *ApJ*, 376, 214
 ——— 1991, *ApJ*, 376, 223
 Blackburn, H.M. & Schmidt, S. 2003, *J. Comp. Phys.*, 186, 610
 Brandenburg, A., Nordlund, A., Stein, R. F., & Torkelsson, U. 1995, *ApJ*, 446, 741
 Chan, C.-K., Psaltis, D., & Ozel, F. 2005, *ApJ*, 628, 353
 ——— 2006, *ApJ*, 645, 506
 Cohl, H.S. & Tohline, J.E. 1999, *ApJ*, 527, 86
 De Villiers, J.-P. & Hawley, J.F. 2003, *ApJ*, 592, 1060
 Don, W.S. & Solomonoff, A. 1997, *SIAM J. Sci. Comput.* 18(4), 1040
 Fleming, T. P., Stone, J. M., & Hawley, J. F. 2000, *ApJ*, 530, 464
 Gammie, C. F., McKinney, J. C., & Tóth, G. 2003, *ApJ*, 589, 444
 Gardiner, T.A. & Stone, J.M. 2005, *J. Comp. Phys.* 205, 509
 Gropp, W., Lusk, E., & Skjellum, A. 1999, *Using MPI: Portable Parallel Programming with the Message-Passing Interface* (2nd ed. Cambridge: The MIT Press)
 Gropp, W., Lusk, E., & Thakur, R. 1999, *Using MPI-2: Advanced Features of the Message-Passing Interface* (2nd ed. Cambridge: The MIT Press)
 Hawley, J.F., Gammie, C.F., & Balbus, S.A. 1995, *ApJ*, 440, 742
 ——— 1996, *ApJ*, 464, 690
 Hawley, J.F., Balbus, S.A., & Winters, W.F. 1999, *ApJ*, 518, 394

Hawley, J.F. 2000, *ApJ*, 528, 462
 ——— 2001, *ApJ*, 554, 534
 Hawley, J.F. & Krolik, J.H. 2001, *ApJ*, 548, 348
 Igumenshchev, I. V., Narayan, R., & Abramowicz, M. A. 2003, *ApJ*, 592, 1042
 Karamanos, G-S. & Karniadakis, G.E. 2000, *J. Comp. Phys.*, 163, 22
 Koide, S., Shibata, K., & Kudoh, T. 1999, *ApJ*, 522, 727
 Kosloff, D., & Tal-Ezer, H. 1993, *J. Comput. Phys.*, 104, 457
 Machida, M., & Matsumoto, R. 2003, *ApJ*, 585, 429
 Mouschovias, T.C. & Paleologou, E.V. 1980, *ApJ*, 237, 887
 Mukhopadhyay, B. 2002, *ApJ*, 581, 427
 Pasquetti, R. 2005, *J. Turbulence*, vol. 6, no. 12, 1
 Pessah, M.E., Chan, C.K., & Psaltis, D. 2006, *MNRAS*, 372, 183
 ———. 2006b, *Phys. Rev. Lett.*, in press (astro-ph/0610565)
 Sagaut, P. 2004, *Large Eddy Simulation for Incompressible Flows: An Introduction* (2nd ed. New York: Springer)
 Shakura, N.I. & Sunyaev, R.A. 1973, *A&A*, 24, 337
 Steinacker, A., & Papaloizou, J. C. B. 2002, *ApJ*, 571, 413
 Stone, J.M., Hawley, J.F., Evans, C.R., & Norman, M.L. 1992, *ApJ*, 388, 415
 Stone, J.M., Hawley, J.F., Gammie, C.F., & Balbus, S.A. 1996, *ApJ*, 463, 656
 Stone, J. M., & Norman, M. L. 1992a, *ApJS*, 80, 791
 ———. 1992b, *ApJS*, 80, 753
 Stone, J.M. & Pringle, J.E. 2001, *MNRAS*, 322, 461